

Article

A Statistical Analysis of Tropical Cyclone-Induced Low-Level Winds near Taiwan Island

Lin Xue ¹ , Ying Li ^{2,*} and Sen Yao ¹¹ School of Finance, Yunnan University of Finance and Economics, Kunming 650221, China² State Key Laboratory of Severe Weather, Chinese Academy of Meteorological Sciences, Beijing 100081, China

* Correspondence: yli@cma.gov.cn

Abstract: Using ERA5 reanalysis data and the tropical cyclone (TC) best track datasets from the China Meteorological Administration and Joint Typhoon Warning Center (from 1979 to 2021), TC-induced low-level winds near Taiwan Island are statistically analyzed. This study mainly concerns TC activity, low-level wind fields around Taiwan Island under TCs, and the detailed characteristics of TC wind structure. Results show that on average, 8.3 TCs enter the study region near Taiwan Island every year mainly from May to November, with more frequent and stronger TCs on the eastern and southern sides of Taiwan Island. For TC centers located at different positions around Taiwan Island, positive and negative vertical vorticity belts alternate between Taiwan Island and the TC center. Moreover, stronger and more frequent TC-induced winds mainly occur on the eastern side of Taiwan Island and the north of Taiwan Strait. TCs to the east of Taiwan Island have stronger maximum sustained wind than those on the western side of the island. Radii of the maximum wind (RMW) for TCs around Taiwan Island range from 5 to 90 nautical mile (nm, 9.3 to 116.7 km) with a mean value of 24.7 nm (44.4 km). Moreover, the RMWs of TCs are the largest (smallest) when the TC centers are located to the southwest (east) of the island. In addition, the outer sizes of TC winds vary from 52 to 360 nm (17.2 to 666.7 km) in the study region, with 187.4 nm (347.1 km) on average, and smaller values for TCs on the western side of the island. The average radii of severe winds, including R_{34} , R_{50} , and R_{64} , are largest in the northeast quadrant and smallest in the southwest quadrant of the TC. The higher the specific wind speed is, the smaller the TC radius and the more symmetric its wind circle. These statistical results may provide references for TC gale forecasting and wind-resistant design for offshore engineering to mitigate TC-induced wind hazards.



Citation: Xue, L.; Li, Y.; Yao, S. A Statistical Analysis of Tropical Cyclone-Induced Low-Level Winds near Taiwan Island. *Atmosphere* **2023**, *14*, 715. <https://doi.org/10.3390/atmos14040715>

Academic Editor: Anthony R. Lupo

Received: 10 February 2023

Revised: 24 March 2023

Accepted: 11 April 2023

Published: 14 April 2023



Copyright: © 2023 by the authors. Licensee MDPI, Basel, Switzerland. This article is an open access article distributed under the terms and conditions of the Creative Commons Attribution (CC BY) license (<https://creativecommons.org/licenses/by/4.0/>).

Keywords: tropical cyclone; low-level wind field; Taiwan Island; wind structure

1. Introduction

Taiwan Island lies between the western North Pacific Ocean and the southeast mainland of China, playing an important role in the marine communications and transportation industries. However, this region is exposed to tropical cyclones (TCs) every year. TCs bring heavy rainfall, storm surges, and high winds, resulting in great losses and hazards to life and property. Among these TC-induced hazards, the high winds not only contribute to heavy rainfall and storm surges but also threaten coastal fisheries, agriculture, maritime transport, and engineering facilities. With the rapid development of the coastal economy, marine development, and increasing population in coastal areas near Taiwan Island, the risk of hazards due to TC-induced winds are increasing, placing higher demands on disaster prevention and mitigation capabilities.

The damage caused by TC-induced winds is closely related to the intensity and structure of the TC. Although the intensity and structure of a TC are related, many factors, such as the movement, environment, boundary structures, and underlying surface, can change the TC intensity and structure. In detail, the maximum winds of a TC occur on the right side of its track [1,2]. Environmental factors such as vertical shear, water vapor conditions, and upper-level divergence can change the intensity and structure of the TC [3–20]. Furthermore, as the wind

hazard occurs in the boundary layer, some specific structures within a TC such as the low-level jet [21–23], rolls [24–32], and small-scale vortices [26,33–39] in the boundary layer can intensify local winds near the surface. In addition, when a TC encounters an island or makes landfall on its path, topographic effects change the low-level wind fields of the TC [40–42]. Major islands off mainland China include Taiwan Island and Hainan Island, as well as many archipelagos, such as the Xisha and Nansha Islands in the coastal area of China. Such topography may induce a low-pressure vortex within the TC circulation or severe weather systems, such as squall lines, thunderstorms, and even tornadoes, which can also trigger wind hazards [40,43]. Previous studies have found that a terrain-induced vortex may occur near the island when a TC approaches Taiwan Island, causing asymmetric TC winds [44–50]. Moreover, the angular flow caused by the obstruction of Taiwan Island and the open channel flow in the Taiwan Strait can also induce a northerly low-level jet in the Taiwan Strait. This jet can shift high winds to the west of the eyewall by advection, resulting in an asymmetric wind field in the TC circulation [42,49,51–56]. In addition, small and medium scale vortices in TCs induced by Hainan Island have been found in previous studies, which could strengthen the local circulation of the TC [57,58]. The TC low-level wind field tends to be more complex and variable over complex topography, which poses challenges for scientific understanding, forecasting, and assessment of TC-induced high winds around the topography.

Previous studies have revealed some characteristics of TC-induced high winds in coastal areas of China. The TC-induced high winds in China mainly occur in the coastal areas east of 105° E, especially in the coastal areas on the south of the Shandong Peninsula [59,60]. TC-induced high winds also have significant seasonal variation and mainly occur in summer and fall. The high winds advance northward from April to August and gradually recede southward from September to November. The maximum TC-induced wind speeds at 10-m height observed by southeastern coastal meteorological stations can all exceed 20.8 m s^{-1} , whereas in inland areas, the maximum wind speeds induced by TCs are much smaller [59].

Some statistical studies of TCs around Taiwan have mainly considered TC frequency, intensity, and TC-induced precipitation [61–63]. There are few studies of TC-induced winds in this region due to the limited situ wind observations. The variation of TC-induced wind fields under the complex topography of the coast and islands needs to be further understood. In this paper, the region near Taiwan Island is taken as the study region (Figure 1a). Using long-term reanalysis data and best track data, TC-induced low-level winds near Taiwan Island are analyzed, including TC activity, low-level wind fields around Taiwan Island under TCs, and the detailed characteristics of TC wind structure.

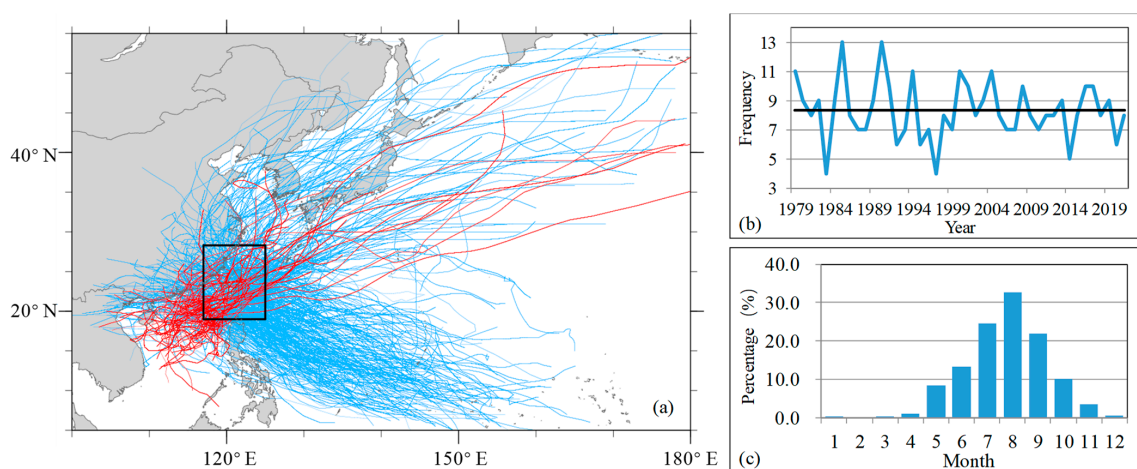


Figure 1. (a) Tracks of TCs that enter the study area (denoted by a black rectangle). Red (blue) lines are TCs generated in the South China Sea (the Northwest Pacific Ocean). (b) Year-to-year (black line denotes the average frequency) variation of TC occurrence frequency and (c) the average percentage of the TC frequency in different months during 1979–2021 in the study area.

The remainder of this paper is organized as follows. Section 2 introduces the methods and data used in this study. Section 3 investigates TC activity around Taiwan Island, the low-level wind fields around Taiwan Island under TCs, and the detailed characteristics of TC wind structure when there are TCs around the island. Conclusions and discussion are given in Section 4.

2. Methods and Data

2.1. Methods

To analyze TC winds around Taiwan Island, the study area (117° E–125° E, 19° N–28.3° N, denoted by the black box in Figure 1a) is centered on Taiwan Island and extends 3° from its coastline. Furthermore, our previous studies have shown that Taiwan Island can induce asymmetrical TC wind fields [48,50] and TC-induced lower-level winds are highly dependent on the relative positions of the TC and Taiwan Island. Therefore, the study area is divided into seven subregions (Figure 2a) based on their position relative to Taiwan Island. The subregions are the northeast (NE), northwest (NW), west (W), southwest (SW), southeast (SE), east (E), and Taiwan Island (TW) (Figure 2a). The study period 1979–2021 is selected to ensure consistent data coverage for analysis of TC activity and low-level wind fields around Taiwan Island under TCs. The detailed wind structure characteristics of TCs are investigated from 2001 to 2021, as the wind structure data provided by the Joint Typhoon Warning Center (JTWC) are only available since 2001.

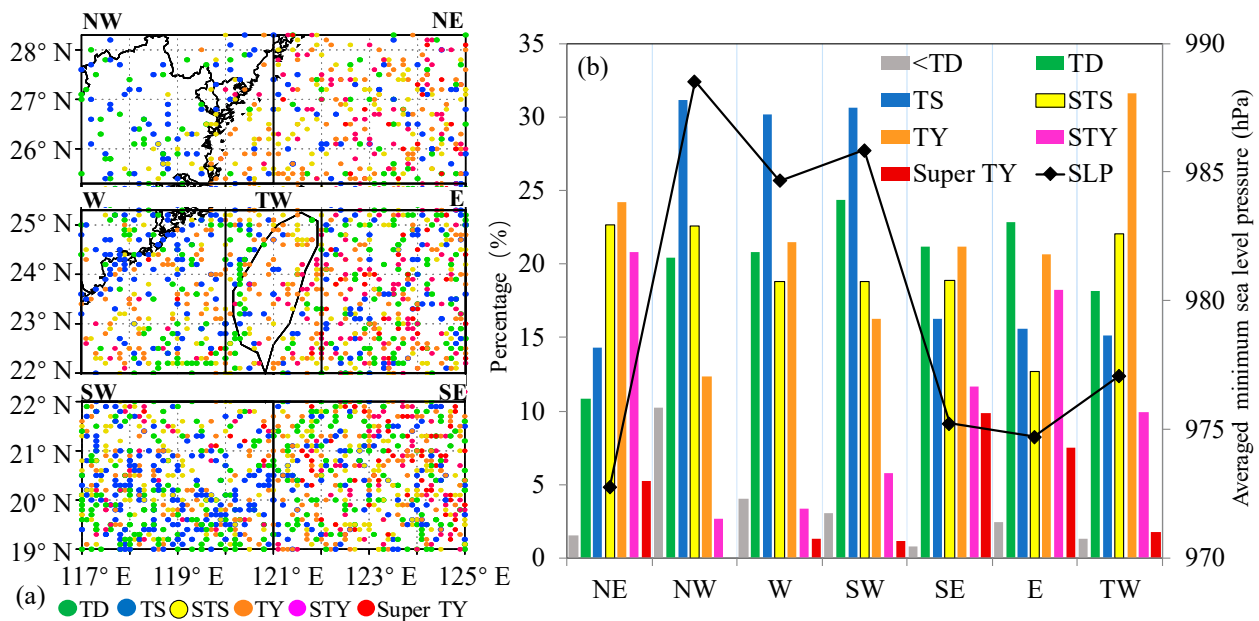


Figure 2. (a) TC samples in different intensity categories from 1979 to 2021. One dot denotes the center of a TC in the study region, and its intensity category is represented by its color, i.e., green dot for Tropical Depression (TD), blue dot for Tropical Storm (TS), yellow dot for severe tropical storm (STS), orange dot for Typhoon (TY), pink dot for severe typhoon (STY), and red dot for Super Typhoon (Super TY). The study area is divided into subregions by black lines (black letters indicate the name of the subregion): northeast of the island (NE), northwest of the island (NW), west of the island (W), southwest of the island (SW), southeast of the island (SE), east of the island (E), and Taiwan Island (TW). (b) Probabilities of TC intensity categories and averaged minimum sea level pressure of TC in each subregion.

2.2. Data

In this study, considering the limitations of TC wind observation at sea, the ERA5 reanalysis data and the best track data provided by the CMA (China Meteorological Administration, https://tcddata.typhoon.org.cn/zjljsjj_sm.html, accessed on 1 September

2022) and JTWC (<https://www.metoc.navy.mil/jtwc/jtwc.html?best-tracks>, accessed on 1 September 2022) are used to investigate the TC-induced low-level wind.

The ERA5 reanalysis dataset has a high temporal and spatial resolution (hourly, 31 km) and provides global estimates of atmospheric, land, and oceanic climate variables (<https://www.ecmwf.int/en/forecasts/dataset/ecmwf-reanalysis-v5>, accessed on 1 September 2022) [64]. In this study, the hourly u and v wind components at 10-m height ($0.25^\circ \times 0.25^\circ$, from 1979 to 2021) provided by ERA5 datasets are used to analyze the low-level TC-induced wind fields in Section 3.2. The ERA5 has been used in many studies of TCs. Its higher resolution has been shown to resolve more TC samples, stronger TC winds, and circulation better than other reanalysis datasets [64–68]. Additionally, the size of outer core TC winds in the ERA5 reanalysis is closer to the observation. However, the ERA5 still underestimates the outer size of TC [66]. Furthermore, the position of the TC center in ERA5 has a smaller displacement error (~ 25 km) relative to the best-track database than other reanalysis datasets [69]. However, ERA5 still underestimates TC-induced high winds at low levels, especially for stronger TCs [67]. Han et al. [70] indicated that the median of the maximum 10-m wind speed bias between ERA5 and the CMA best track data for TCs affecting Shanghai varies from 4.4 to 5.2 m s^{-1} near the eastern coast, and the median of the 10-m wind direction bias is in the range of -7° to 7° . Nevertheless, considering the long time series and global coverage of the ERA5 dataset, it can make up for the scarcity of offshore TC wind field observations and provide information to help reveal the characteristics of TC-induced winds in the study area.

The CMA best track dataset from 1979 to 2021 is used to analyze TC activity in Section 3.1, provide the location of the TC center in Section 3.2, and analyze the maximum sustained surface wind (MSW) in Section 3.3. This best track dataset contains the basic-track information at 6-hourly intervals along TC tracks, including the location, the minimum sea level pressure, and the MSW near the TC center (2-min mean at 10-m height recorded as a synthesis of observations such as in situ surface observations, aircraft reconnaissance, satellite imagery, ship reports, and island observations.). TC intensity is classified into six categories depending on the 2-min mean MSW [71]: tropical depression (TD; 10–17 m s^{-1}), tropical storm (TS; 18–24 m s^{-1}), severe tropical storm (STS; 25–33 m s^{-1}), typhoon (TY; 34–41 m s^{-1}), severe typhoon (STY; 42–51 m s^{-1}), and super typhoon (Super TY; stronger than 51 m s^{-1}). Note that some new observation sources, such as aircraft, satellite, and radar observations, have been gradually added to the dataset since 1949. These changes may influence the best-track data over the open ocean, especially the extreme intensity values [71]. Therefore, this study is conducted for the 1979–2021 period when the observation sources are more consistent.

To reveal the detailed characteristics of TC wind structure around Taiwan Island, the JTWC best track dataset from 2001 to 2021 is used in Section 3.3. The dataset contains basic information such as the location of the TC center, minimum sea level pressure, maximum sustained wind speed (1-min mean), and TC development level every 6 h. In addition, it provides structural information including the radius of maximum wind (RMW), radius of the last closed isobar in nm (ROCI), the shape and radii of the specific winds (34, 35, 50, or 64 kt) since 2001. Note that the records for the 34-kt winds have been quality controlled. Additionally, it has an average error of 20–40 nm, which equates to approximately 15–30% of the climatological mean R_{34} (130 nm) for this dataset [72,73]. Moreover, the JTWC wind radii are considered to be generally larger in the best tracks [74]. In addition, the 50- and 64-kt radii are computed via linear regression from the radius of 34-kt winds. R_{34} is more reliable than those for 50-kt and 64-kt winds. Although there are some quality issues of wind radii in the JTWC best track data set [72,73,75,76], the JTWC dataset can provide the most reliable and continuous wind radii data on the sea [77]. The shape parameter of a specific wind field could be a full circle, semicircle, or quadrant. In the study region near Taiwan Island, the shapes of specific wind fields are NEQ (the northeast quadrant) for all samples, indicating that high winds mainly occur in the northeast quadrant of the TC

circulation. Furthermore, the radii in the four quadrants of the specific wind circles are recorded in the order of northeast, southeast, southwest, and northwest.

3. Results

3.1. Tropical Cyclone Activity

The frequency of TC-induced winds is highly related to TC activity. During the study period, 358 TCs passed through the study region (Figure 1a, from the CMA best track dataset). Of these TCs, 17% originated in the South China Sea (considered as the ocean to the west of 120° E, red lines in Figure 1a) and 83% are from the western Pacific Ocean (blue lines in Figure 1a). Most of their paths are northwestward or northwest-turning (Figure 1a). Figure 1b shows the inter-annual variation of TC frequency in the study area. The interval between the two peaks is approximately 5 years, and 8.3 TCs entered the region every year on average. The maximum annual frequency of TCs is 13, which occurred in 1985 and 1990, whereas in 1983 and 1997, only 3 TCs entered the study area. The frequency of TCs entering the study area also shows a monthly variation (Figure 1c). TCs in the study region can occur throughout the year, except for February, and are concentrated mainly from May to November. The occurrence rate of TCs gradually increases from April, reaching a peak in August (32.8% of TCs in the whole year), and then gradually decreases. Previous studies have shown that the significant seasonal differences in TC activity are closely related to the monsoon activity of the region [61,78,79].

The records of TCs provided by the CMA best track dataset are at 6-h intervals. Every record is taken as a sample in the following investigations, so there are 2537 records in the study area from 1979 to 2021 (dots in Figure 2a). The sample sizes of TC records in each subregion are 254 for subregion NE, 169 for NW, 238 for W, 502 for SW, 530 for SE, 359 for E, and 194 for TW, respectively. Most samples tend to be concentrated on the southern and eastern sides of Taiwan Island (i.e., SW, SE, and E), whereas the numbers of samples are smaller on the northern and western sides (i.e., NW, NE, and W). The highest (lowest) number of samples is in subregion SE (NW). Furthermore, the intensity categories of TC samples are different in each subregion (Figure 2b). Stronger TCs tend to occur over Taiwan Island and its eastern side (the subregions TW and NE, SE, E), whereas to the west, TC intensity is much weaker (Figure 2b).

TC activity around Taiwan Island varies in both frequency and intensity, indicating that the topography of this island may have some effect on the TCs around it. Since TC-induced low-level winds are closely related to the frequency and intensity of the TC, the wind characteristics in different directions off Taiwan Island will be investigated further.

3.2. Wind Field around Taiwan Island under a Tropical Cyclone

To reveal the spatial variance of TC-induced winds around Taiwan Island, the 10-m wind field around the island is investigated by composite analysis. Wind fields provided by ERA5 are analyzed for TC samples in the same subregion from 1979 to 2021. Note that the wind field data provided by ERA5 cannot resolve the TC circulation, and the wind speed is underestimated (more details in Section 2.2). ERA5 cannot completely resolve the inner core wind structure of TC owing to its horizontal spatial resolution (31 km). In addition, wind variables are averaged for all TC samples in the same subregion in the composite analysis, resulting in errors in describing the composite field near the TC center. TC outer-core winds are distributed from the eyewall to the edge of the TC circulation, with wind speeds decreasing outwards from the radius of maximum wind. Therefore, the wind field characteristics shown in this section are mainly for TC outer-core winds, but they can still provide references for wind forecasting or evaluation beneath TCs in the study region.

3.2.1. Vertical Vorticity and Wind Speed in the Lower Layer

Both the composite vertical vorticity and wind fields are asymmetric at 10-m height for TCs located in different directions off Taiwan Island (Figure 3). Positive and negative vorticity belts in the TC circulation are distributed alternately around Taiwan Island, except

for TCs in subregion TW (shaded in Figure 3). Belts of negative vorticity appear in the region between the TC center and Taiwan Island, whereas the positive belts are located on the other side of Taiwan Island and beside the areas near the TC center. Vorticity belts shift with the relative location between the TC and Taiwan Island, indicating a close relation to the topography of the island. When the TC center is over Taiwan Island (Figure 3d), negative vorticity bands are distributed over the Taiwan Strait and the northwestern side of Luzon Island. Furthermore, for TCs in subregions TW, E, SW, and SE, a negative vorticity band appears along the coastline of mainland China. This may be attributed to the frictional deceleration induced by the land.

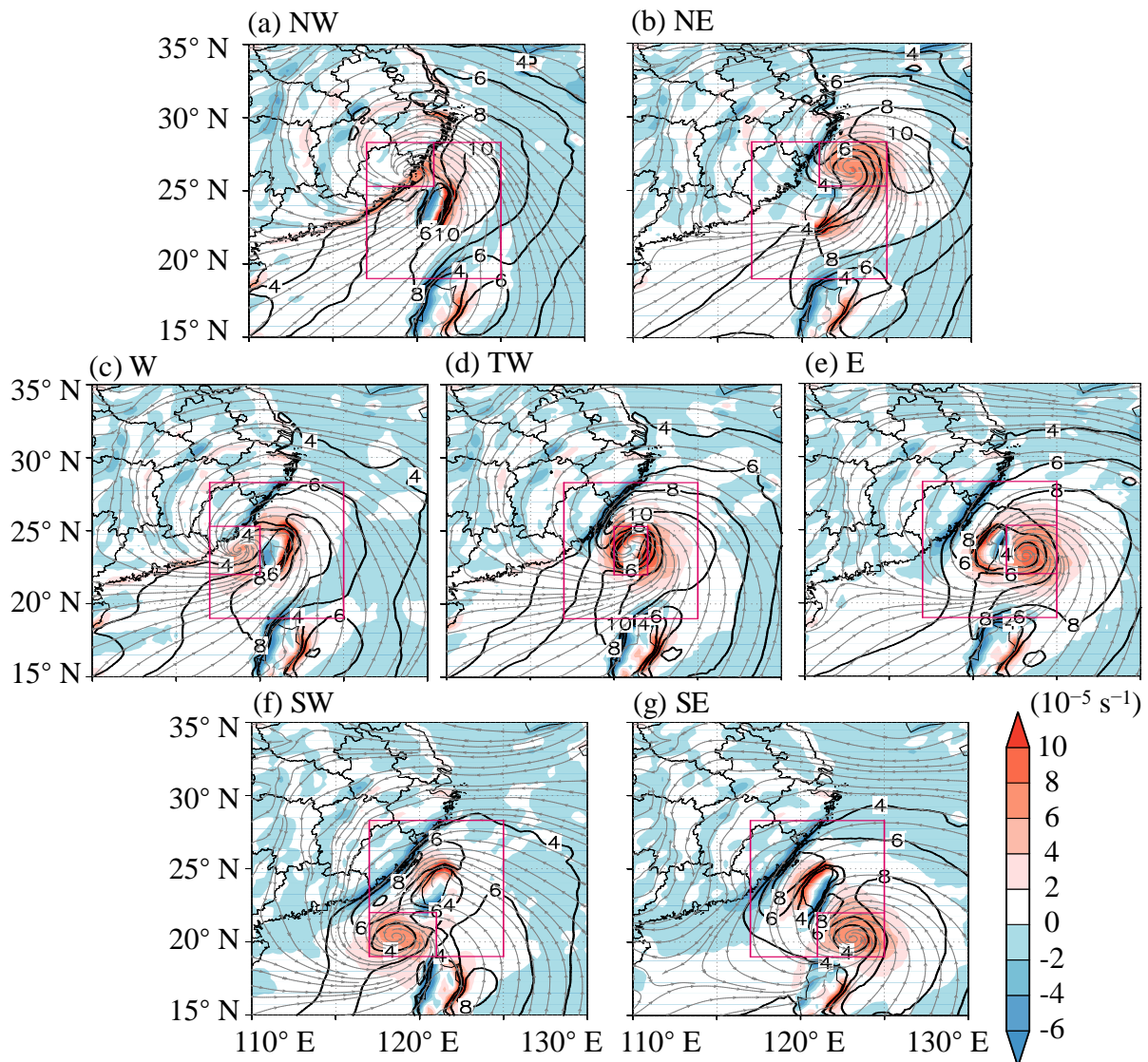


Figure 3. Composite vertical vorticity (shading, units: 10^{-5} s^{-1}), wind speed (black contours, units: m s^{-1}), and streamlines (gray lines) at 10-m height for TCs in subregions: (a) NW, (b) NE, (c) W, (d) TW, (e) E, (f) SW, and (g) SE. Here and in Figure 4, the outer box indicates the study region and the nested box indicates the composite subregion.

Vertical vorticity is the reflection of inhomogeneous wind distribution. Stronger winds generally appear to the east of the island when TC centers are around Taiwan Island (Figure 3). Stronger winds may extend into the Taiwan Strait. Previous studies have suggested that this is closely related to the channeling effect of the Taiwan Strait [49,54]. Winds over the land are much weaker.

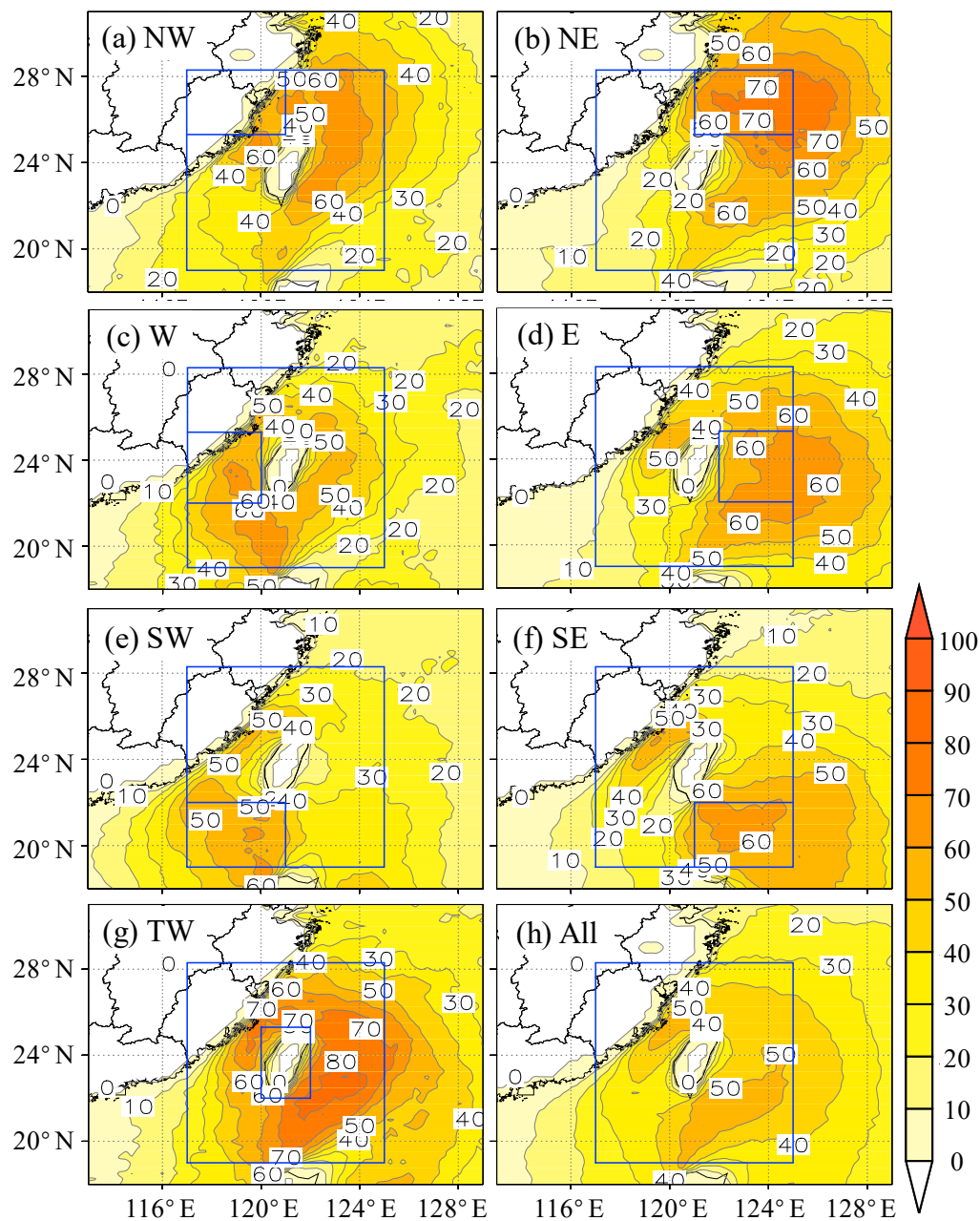


Figure 4. Percentage of the occurrence frequency of strong wind at 10-m height for wind speed exceeding 10 m s^{-1} in (a–g) subregions and (h) all samples (All).

3.2.2. Occurrence Frequency of Severe Winds

A TC-induced gale is usually defined as TC-induced severe winds at 10-m height with 10-min (2-min) mean maximum wind speed higher than 10.8 m s^{-1} (17.2 m s^{-1}) in meteorological station observations (the Tropical Cyclone Yearbook provided by the CMA). Given that ERA5 underestimates TC gales [64–66,68], 10 m s^{-1} was used as the threshold for TC severe wind in this section. The occurrence frequency ratio is defined as the percentage of numbers exceeding 10 m s^{-1} divided by the sample size in a grid cell. The occurrence frequency ratios of wind speeds exceeding 10 m s^{-1} at 10-m height are calculated for every grid cell ($0.25^\circ \times 0.25^\circ$) for TCs in each subregion to characterize TC-induced strong wind around Taiwan Island qualitatively (Figure 4).

When the TC center is around Taiwan Island, the strong wind exceeding 10 m s^{-1} is concentrated mainly to the east of Taiwan Island and the Taiwan Strait ($>50\%$, Figure 4h). This indicates that these regions are exposed to higher risk from TC-induced severe wind.

When TC centers are located to the north of Taiwan Island (Figure 4a,b), the occurrence frequency ratio of strong wind northeast of Taiwan Island is >60%. When TC centers are over Taiwan Island (Figure 4g), the occurrence frequency ratio of the wind speed exceeding 10 m s^{-1} is >80% east of the island and >70% in the Taiwan Strait. In addition, the occurrence rate of TC-induced severe winds over Taiwan Island is smaller than that over the surrounding sea areas. This may be attributed to the frictional deceleration effect of the rough surface of the island [44,48,50,80].

3.3. Characteristics of TC Wind Structure

The damage of TC-induced wind relates to the TC intensity, wind structure, and its extent. In this section, some detailed characteristics of the TC-induced wind are investigated. Firstly, as the most severe or dangerous winds induced by TCs are usually within the eyewall, their intensity (the maximum sustained wind near the TC center, MSW) and the location (the Radius of Maximum Wind, RMW) are analyzed. Moreover, the radius of the outermost closed isobar (ROCI) which could indicate the TC outer wind size is explored. In addition, the size and shape of 34-kt, 50-kt, and 64-kt wind circles are closely related to the degrees and extent of TC-induced wind damage. Thus, the radii of 34-kt, 50-kt, and 64-kt winds and their asymmetry are further investigated for TCs near Taiwan Island.

3.3.1. Maximum Winds

The MSW near the TC center provided by best track datasets shows the best accuracy compared with other types of datasets, especially over the sea. The MSW (2-min mean) from the CMA best track dataset for 1979–2021 is used to investigate the maximum TC-induced wind near Taiwan Island. Taking each 6-h record in the study region as a sample, there are 2537 samples in total. In the whole study region near Taiwan Island, the MSW varies from 9 to 75 m s^{-1} , with a mean value of 28.1 m s^{-1} . Subregions in different directions from Taiwan Island have different MSWs (Figure 5a). In general, subregions on the east of Taiwan Island have more severe winds than western regions. The average MSW for each subregion is strongest (weakest) in SE (NW), and the maximum MSW (75 m s^{-1}) is also located in the SE. On the western side of Taiwan Island, the mean value and the median of MSW in subregion W (24.5 m s^{-1} mean and 23 m s^{-1} median) are higher than those in the NW (22.1 m s^{-1} mean and 20 m s^{-1} median) and SW (24.4 m s^{-1} mean and 20 m s^{-1} median).

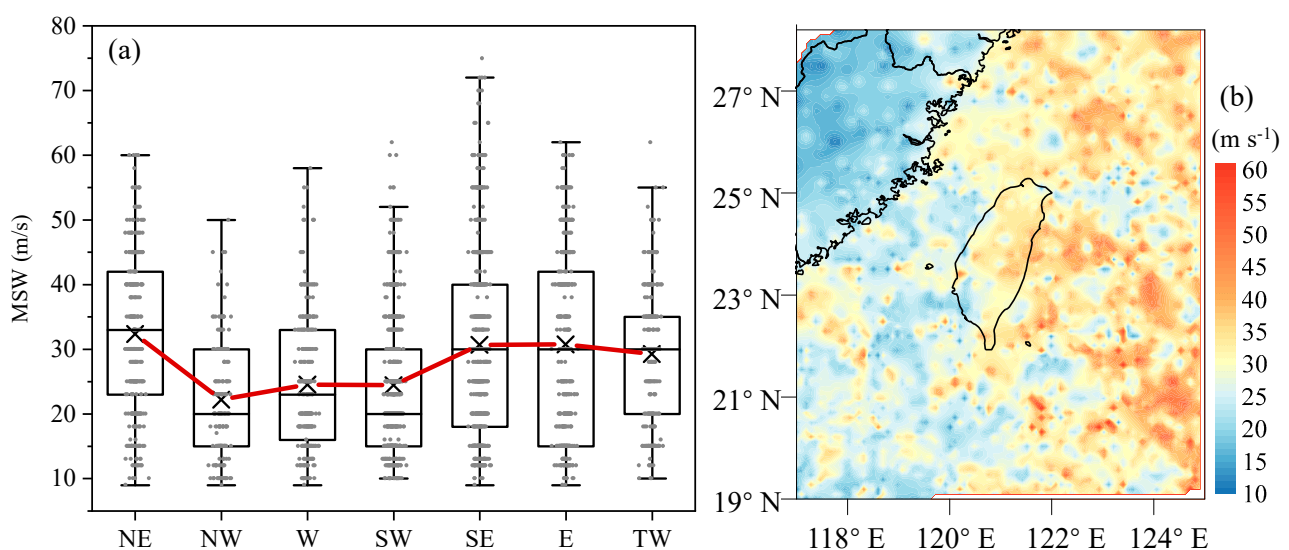


Figure 5. (a) Box plot of MSW (unit: m s^{-1}) in subregions (black crosses and the red line indicate the mean value for each subregion) and (b) spatial distribution of the MSW near Taiwan Island from 1979 to 2021 (unit: m s^{-1}).

In addition, samples of the MSW at 10-m height are interpolated onto a field in the study area (resolution $0.1^\circ \times 0.1^\circ$) using Kriging interpolation [81] (Figure 5b). The MSW of TCs over the sea is generally greater than that in mainland areas and decreases significantly from ocean to land. The MSW on the eastern side of Taiwan Island is generally greater than that on the western side. MSWs within the Taiwan Strait are generally smaller than 35 m s^{-1} . High wind speeds also occur on the northern and southern sides of the Taiwan Strait. The MSW over Taiwan Island is mainly distributed between 20 and 40 m s^{-1} , which is greater than that over mainland China on the western coast of the Taiwan Strait. Moreover, the MSW is larger to the north of the island than on the southern side. Note that the MSW is located at the RMW, but it is interpolated to the location of the TC center in this study. Using the mean value of RMW in the study area (see Section 3.2.2), the average error in the position of MSW is about 42.5 km (about 0.4°) in the study area.

3.3.2. Radius of Maximum Winds

The strongest TC-induced winds are found at the RMW. The RMW is important for analyzing the damaging wind induced by TCs. The JTWC best track datasets have recorded RMW since 2001. Every record in a 6-h interval within the study area is considered as a sample. There are 1813 samples in the study region near Taiwan Island during 2001–2021. The RMW varies from 5 nm (45 samples) to 90 nm (only 1 sample). The mean and median values of RMW are 24.7 nm (45.83 km) and 20 nm, respectively. The lower quantile (25%) of RMW is 15 nm and the upper quantile (75%) is 30 nm. In detail, 17.7% of samples are within 15 nm, which has the maximum sample size (345 samples) for all RMW values (Figure 6a). The region-mean value of RMW (Figure 6b) is largest in subregion SW (31.5 nm) and smallest in subregion E (21 nm). The RMW for regions on the western side (subregions W, SW, NW) of the island is larger than for the regions on the eastern side (subregions E, SE, NE). Samples with RMW larger than 50 nm are concentrated mainly in subregions W and SW. There are more TCs with RMW smaller than 10 nm in subregions NE, TW, and E.

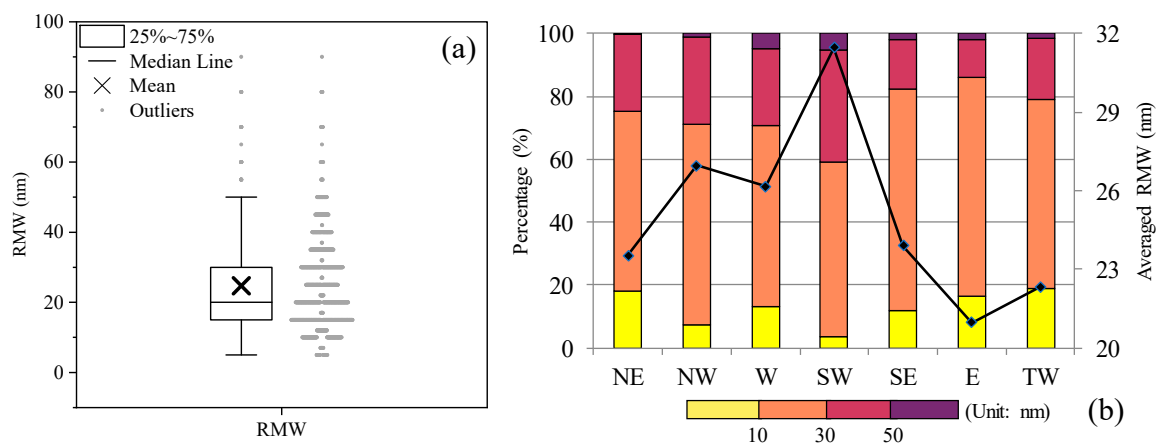


Figure 6. (a) Box plot of RMW (unit: nm). The samples are showed with gray dots on the right of the box. (b) Percentages of samples with different RMW (bars; yellow: $\text{RMW} \leq 10 \text{ nm}$; orange: $10 \text{ nm} < \text{RMW} \leq 30 \text{ nm}$; red: $30 \text{ nm} < \text{RMW} \leq 50 \text{ nm}$; purple: $\text{RMW} > 50 \text{ nm}$) and the average RMW (right axis, black line, unit: nm) in the subregions during 2001–2021.

3.3.3. Radius of the Outermost Closed Isobar

The TC outer wind size represents the extent of TC severe winds. It has received increasing attention since it is important for some hazards, such as storm surges and tornadoes. Operationally, TC outer wind size is typically characterized by the radius of the outermost closed isobar (ROCI) [82,83]. Using the JTWC best track dataset from 2001 to 2021, a ROCI record with a 6-h interval in the study area is considered as a sample to investigate the size of TC outer winds. There are 1814 samples for ROCI in the study region from 2001 to 2021. The mean and the median values of ROCI are 187.4 and 190 nm for all

samples (Figure 7, red box), and the ROCI varies from 52 to 360 nm. Based on the mean and median of ROCI in each subregion around Taiwan Island, the size of the TC outer winds is smaller on the western side of Taiwan Island and tends to be larger on the eastern side (Figure 7, black boxes). The regional mean value of ROCI in subregion W (E) is the smallest (largest) at 163.3 nm (201 nm).

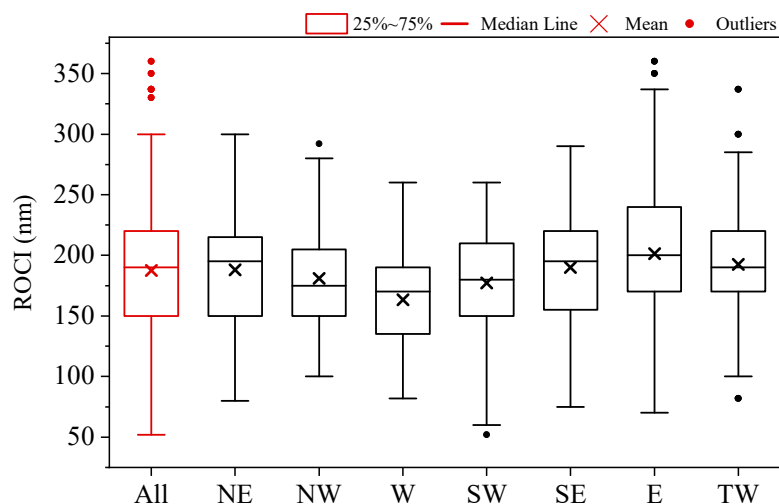


Figure 7. Box plot of ROCI (units: nm). The box with a red outline is for all samples in the study region, and those with black outlines are for samples in each subregion.

3.3.4. Radius of Specific Winds and Asymmetry

The size or extent of severe winds in TC is important in forecasting, disaster prevention, and mitigation for TC-induced hazards. Using the shape and radii of 34-kt (R_{34}), 50-kt (R_{50}), and 64-kt (R_{64}) winds provided by the JTWC best track dataset since 2001, the area subject to severe TC-induced winds is analyzed. Although radii of 35-kt winds are also provided by JTWC, they are not discussed in this study because of their limited sample size. One record within a 6-h interval in the study area is considered as a sample. There are 811, 529, and 377 radius samples for the 34-kt, 50-kt, and 64-kt winds, respectively, and 1717 samples in the whole study area from 2001 to 2021. The shapes of specific winds are NEQ for all samples in the study region, indicating high winds occur mainly in the northeast quadrant of the TC circulation.

The average R_{34} , R_{50} , and R_{64} in the northeast, southeast, southwest, and northwest quadrants of TCs in each subregion are shown in Figure 8. The average radii for all samples in each quadrant are largest in the northeast quadrant and smallest in the southwest quadrant (bars with black outline in Figure 8). The higher the specific wind speed, the shorter its radius. The R_{34} varies from 86.9 to 136 nm and the R_{50} ranges between 63.7 and 69.2 nm, whereas the R_{64} is within the range 25.7 to 46.2 nm. Subregions in different directions around Taiwan Island have different radii of specific winds. The radius of specific winds generally tends to be larger over or east of Taiwan Island than to the west. In addition, the differences between each subregion for R_{50} and R_{64} in the four quadrants are smaller than those for R_{34} . R_{50} and R_{64} are the shortest for subregion W in four quadrants. The R_{34} of subregion SW is the smallest in all quadrants except for the northwest quadrant (R_{34} in subregion W is the smallest in this quadrant). For all subregions in all four quadrants, R_{34} in subregions NE and TW are the largest for the eastern (i.e., the northeast and southeast quadrants) and western (including the northwest and southwest quadrants) sectors, respectively. R_{50} and R_{64} are the largest for samples in subregions SE and SW. Furthermore, there is a smaller deviation between the eastern and southern sectors for both R_{50} and R_{64} . This may be attributed to the fact that more intense TCs have a more compact and symmetrical structure.

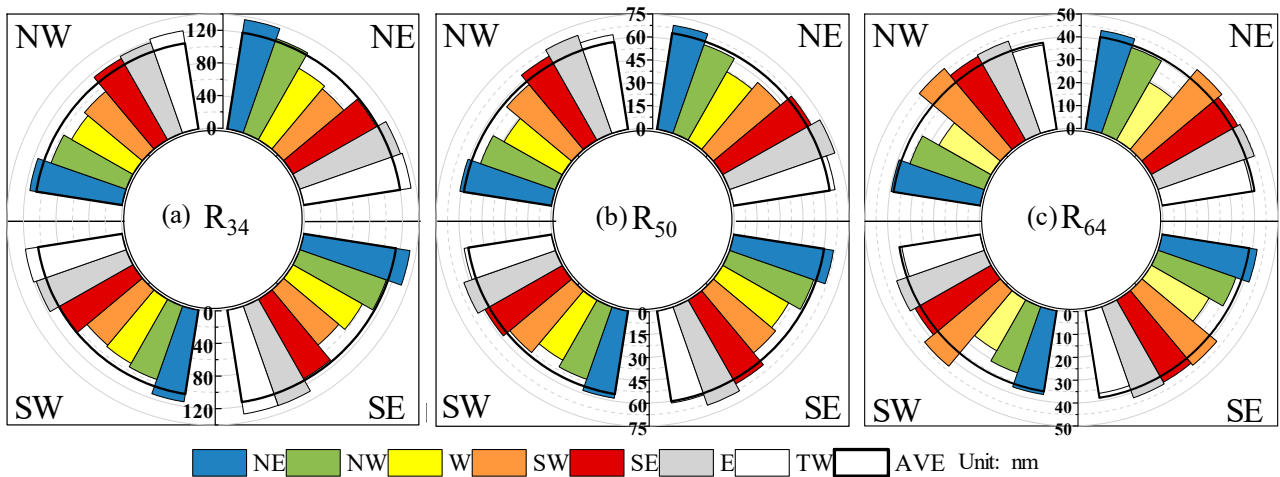


Figure 8. Average radii of (a) 34-kt, (b) 50-kt, and (c) 64-kt wind in four quadrants for TCs in each subregion (unit: nm). The thick black outline is the average radius for all samples in each quadrant.

To quantify further the asymmetry of TCs in different subregions around Taiwan Island, the wind asymmetry (α) defined by Song and Klotzbach [8] is analyzed:

$$\alpha = \frac{1}{2} \sqrt{(R_{NE} - R_{SW})^2 + (R_{SE} - R_{NW})^2}, \quad (1)$$

where R_{NE} , R_{SW} , R_{SE} , and R_{NW} are the radii in the northeast, southwest, southeast, and northwest quadrants, respectively. When the wind field of the TC is symmetric, α will be zero. Additionally, a larger α indicates a more asymmetric TC wind structure.

The α (Figure 9) in each subregion is calculated by the radius in each quadrant for R_{34} (black box), R_{50} (blue box), and R_{64} (red box). α for R_{34} is larger than for R_{50} and R_{64} , indicating that the stronger TC-induced wind is more symmetric. Moreover, there are differences in asymmetry for TCs in different directions around Taiwan Island. For R_{34} and R_{50} , TCs on the northern side of Taiwan Island tend to be more asymmetric than the TCs on the southern side. The median of the asymmetry factor α indicates that R_{34} , R_{50} , and R_{64} are most asymmetric in subregion NW and most symmetric in subregion W.

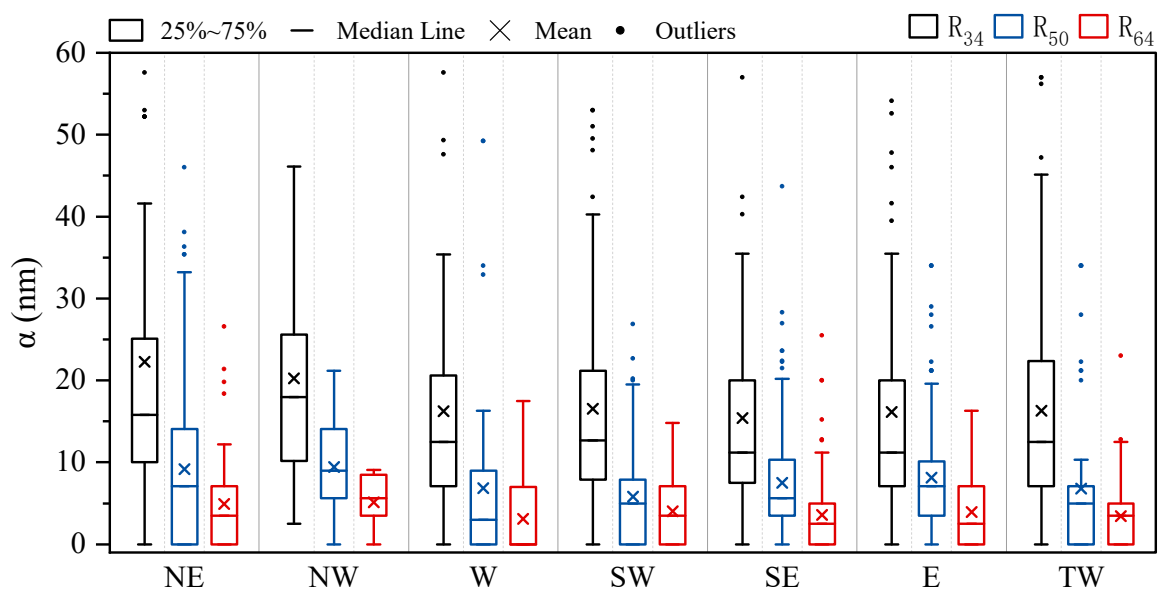


Figure 9. Box plot of the asymmetry factor α (units: nm) for R_{34} (black boxes), R_{50} (blue boxes), and R_{64} (red boxes) in subregions near Taiwan Island.

4. Conclusions and Discussion

The above results demonstrate that the frequency, intensity, and wind structure of TCs vary with the position of their centers around Taiwan Island. TCs on the eastern side of the island are more frequent, severe, and symmetric. Moreover, they tend to have larger outer-core wind size and more compact inner-core winds. Due to the limited long-term observation of TC winds at sea, there are few statistical studies of TC wind characteristics at sea, especially for the offshore region near an island. This work has revealed these statistical wind characteristics for TCs around Taiwan Island by taking advantage of 43-year best track data and reanalysis dataset. The results could provide references for TC forecasting, offshore engineering wind-resistant design, maritime transportation, and so on. In particular, we found that belts of positive and negative vertical vorticity within the TC circulation are distributed alternately around the island when TC centers are located at different locations around Taiwan Island. This phenomenon demonstrates the inhomogeneity of wind fields under TCs, which needs to be considered in forecasting or evaluating TC winds around the island.

This work has mainly revealed the statistical characteristics. A few mechanisms behind the phenomenon are investigated. Although these are based on previous studies, we can still try to understand the physical mechanism behind these results. As there are differences in low-level wind fields when TCs are located in different positions relative to Taiwan Island, the structure of TC-induced low-level winds is closely related to the topography of Taiwan Island and its surroundings. The Central Mountain range on Taiwan Island has an average altitude of ~3000 m and an area of 300 km × 100 km. Its high altitude and large size make the topographic effect of Taiwan Island more notable than that of other islands. In previous studies, the asymmetric TC wind fields are attributed to the frictional deceleration, the channeling effect, and the displacement of the flow caused by the topography of Taiwan Island [48–50,55,56].

This study has found that the positive and negative vertical vorticity belts in the TC circulation are distributed alternately around the island when TC centers are located at different positions relative to Taiwan Island. Our previous studies of Typhoon Meranti (1010) indicated that the topography of Taiwan could induce a pair of mesoscale vortices, giving positive and negative vorticity belts in the TC circulation [48,50]. These structures help to intensify the vertical motion and increase TC kinetic energy in the circulation system of the TC after it enters the Taiwan Strait. The mesoscale systems disappear if the topography of Taiwan is removed. Similar vorticity belts could be also found near Hainan [84] and Luzon Island (in Figure 3). Therefore, the positive and negative vorticity belts in the TC circulation may be attributed to the topography of Taiwan Island.

The TC wind structure around Taiwan Island is characterized by TCs east of the island tending to have more intense MSW, larger outer-core wind extent, more compact inner-core winds, and a more symmetric wind field. As the TC structure depends on its intensity, the structure of TC wind for TCs on the eastern side of the island may be closely related to their greater intensity. In general, a more intense TC is considered to have a more symmetrical circulation and more compact inner-core structure. The movement, environment, boundary structures, and underlying surface properties can change the TC intensity in regions near Taiwan Island (more details in Section 1). Furthermore, the RMW, ROCI, R_{34} , R_{50} , and R_{64} analyzed in this work are parameters of TC size, which is important for the distribution and extent of damaging TC-induced winds. The inner-core size such as the RMW is thought to be closely related to its initial vortex size [83,85–87]. Some studies have suggested that secondary eyewall formation, the eyewall replacement cycle, transition to an annular structure [88], and some synoptic environments, such as the vertical shear [89], rich moisture [11,90–93], and surface entropy flux [91], may lead to an increase in the inner-core size. Expansion of the outer core depends on its initial size [91,93] and the diurnal cycle [68,94] and is influenced by environmental factors such as the vertical shear [95–99], dry mid-tropospheric air [100], and sea surface temperature [101,102]. Moreover, the land can also reduce the TC outer size monotonically and rapidly after landfall, especially for a

rough surface [103–105]. In addition, owing to the frictional gradient between ocean and land, the wind fields in the rear and left-of-motion quadrants decay the fastest [106]. This may account for the smaller sized TCs on the western side of Taiwan Island.

TC-induced wind hazards are highly related to the activity, intensity, and structure of the TC. The many complex factors and the interaction between TC intensity and structure changes remain important research questions for TC wind characteristics, especially for regions with complex terrain. Thus, additional research investigating the physical mechanisms behind the statistical results needs to be conducted to advance our knowledge of TC-induced winds.

Author Contributions: Conceptualization, L.X. and Y.L.; methodology, L.X. and Y.L.; software, L.X. and Y.L.; validation, L.X. and Y.L.; formal analysis, L.X.; investigation, L.X.; resources, L.X. and S.Y.; data curation, L.X. and S.Y.; writing—original draft preparation, L.X.; writing—review and editing, L.X. and Y.L.; visualization, L.X. and S.Y.; supervision, L.X. and Y.L.; project administration, L.X.; funding acquisition, L.X. and Y.L. All authors have read and agreed to the published version of the manuscript.

Funding: This research was funded by the National Natural Science Foundation of China (NSFC) (No. 42005141, 41930972), Yunnan Fundamental Research Projects (No. 202001AU070089), Key Research and Development Plan of Yunnan Province (202203AC100003), and Financial Innovation Center of Southwestern University of Finance and Economics (No. FIC2021C0012).

Institutional Review Board Statement: Not applicable.

Informed Consent Statement: Not applicable.

Data Availability Statement: The ERA-5 data can be downloaded from the website <https://www.ecmwf.int/en/forecasts/datasets/reanalysis-datasets/era5> (accessed on 2 February 2023). The tropical cyclone (TC) best track dataset can be downloaded from the China Meteorological Administration (CMA) (https://tcdata.typhoon.org.cn/zjljsjj_sm.html) (accessed on 2 February 2023) and Joint Typhoon Warning Center (JTWC) (<https://www.metoc.navy.mil/jtwc/jtwc.html?best-tracks>) (accessed on 2 February 2023).

Acknowledgments: The authors would like to express their sincere gratitude to the reviewers and editors for their constructive comments and helpful suggestions.

Conflicts of Interest: The authors declare no conflict of interest.

References

1. Hughes, L.A. On the low-level structure of tropical storms. *J. Atmos. Sci.* **1952**, *9*, 422–428.
2. Miller, B.I. Characteristics of Hurricanes: Analyses and calculations made from measurements by aircraft result in a fairly complete description. *Science* **1967**, *157*, 1389–1399. [[CrossRef](#)] [[PubMed](#)]
3. Gray, W.M. The mutual variation of wind, shear, and baroclinicity in the cumulus convective atmosphere of the hurricane. *Mon. Weather Rev.* **1967**, *95*, 55–73. [[CrossRef](#)]
4. DeMaria, M. The effect of vertical shear on tropical cyclone intensity change. *J. Atmos. Sci.* **1996**, *53*, 2076–2088. [[CrossRef](#)]
5. Rogers, R.; Uhlhorn, E. Observations of the structure and evolution of surface and flight—Level wind asymmetries in Hurricane Rita (2005). *Geophys. Res. Lett.* **2008**, *35*, L22811. [[CrossRef](#)]
6. Tang, B.; Emanuel, K. Midlevel ventilation's constraint on tropical cyclone intensity. *J. Atmos. Sci.* **2010**, *67*, 1817–1830. [[CrossRef](#)]
7. Tang, B.; Emanuel, K. Sensitivity of tropical cyclone intensity to ventilation in an axisymmetric model. *J. Atmos. Sci.* **2012**, *69*, 2394–2413. [[CrossRef](#)]
8. Song, J.; Klotzbach, P.J. Wind structure discrepancies between two best track datasets for western North Pacific tropical cyclones. *Mon. Weather Rev.* **2016**, *144*, 4533–4551. [[CrossRef](#)]
9. Klotz, B.W.; Jiang, H. Examination of surface wind asymmetries in tropical cyclones. Part I: General structure and wind shear impacts. *Mon. Weather Rev.* **2017**, *145*, 3989–4009. [[CrossRef](#)]
10. Tao, D.; Zhang, F. Evolution of dynamic and thermodynamic structures before and during rapid intensification of tropical cyclones: Sensitivity to vertical wind shear. *Mon. Weather Rev.* **2019**, *147*, 1171–1191. [[CrossRef](#)]
11. Hill, K.A.; Lackmann, G.M. Influence of environmental humidity on tropical cyclone size. *Mon. Weather Rev.* **2009**, *137*, 3294–3315. [[CrossRef](#)]
12. Fujiwara, K.; Kawamura, R.; Hirata, H.; Kawano, T.; Kato, M.; Shinoda, T. A positive feedback process between tropical cyclone intensity and the moisture conveyor belt assessed with Lagrangian diagnostics. *J. Geophys. Res. Atmos.* **2017**, *122*, 502–512, 521. [[CrossRef](#)]

13. Riehl, H. A model of hurricane formation. *J. Appl. Phys.* **1950**, *21*, 917–925. [[CrossRef](#)]
14. DeMaria, M.; Kaplan, J.; Baik, J.-J. Upper-level eddy angular momentum fluxes and tropical cyclone intensity change. *J. Atmos. Sci.* **1993**, *50*, 1133–1147. [[CrossRef](#)]
15. Molinari, J.; Skubis, S.; Vollaro, D. External influences on hurricane intensity. Part III: Potential vorticity structure. *J. Atmos. Sci.* **1995**, *52*, 3593–3606. [[CrossRef](#)]
16. Molinari, J.; Skubis, S.; Vollaro, D.; Alsheimer, F.; Willoughby, H.E. Potential vorticity analysis of tropical cyclone intensification. *J. Atmos. Sci.* **1998**, *55*, 2632–2644. [[CrossRef](#)]
17. Li, Y.; Guo, L.-x.; Ying, Y.; Hu, S. Impacts of upper-level cold vortex on the rapid change of intensity and motion of Typhoon Meranti (2010). *J. Trop. Meteor.* **2012**, *18*, 207–219.
18. Wei, N.; Li, Y.; Zhang, D.-L.; Mai, Z.; Yang, S.-Q. A statistical analysis of the relationship between upper-tropospheric cold low and tropical cyclone track and intensity change over the western North Pacific. *Mon. Weather Rev.* **2016**, *144*, 1805–1822. [[CrossRef](#)]
19. Guo, Y.-P.; Tan, Z.-M. Westward migration of tropical cyclone rapid-intensification over the Northwestern Pacific during short duration El Niño. *Nat. Commun.* **2018**, *9*, 1507. [[CrossRef](#)]
20. Wen, D.; Li, Y.; Zhang, D.-L.; Xue, L.; Wei, N. A statistical analysis of tropical upper-tropospheric trough cells over the western North Pacific during 2006–2015. *J. Appl. Meteorol. Climatol.* **2018**, *57*, 2469–2483. [[CrossRef](#)]
21. Powell, M.D. The transition of the Hurricane Frederic boundary-layer wind field from the open Gulf of Mexico to landfall. *Mon. Weather Rev.* **1982**, *110*, 1912–1932. [[CrossRef](#)]
22. Korolev, V.; Petrichenko, S.; Pudov, V. Heat and moisture exchange between the ocean and atmosphere in tropical storms Tess and Skip. *Sov. Meteor. Hydrol.* **1990**, *3*, 92–94.
23. Franklin, J.L.; Black, M.L.; Valde, K. GPS dropwindsonde wind profiles in hurricanes and their operational implications. *Weather Forecast.* **2003**, *18*, 32–44. [[CrossRef](#)]
24. Wurman, J.; Winslow, J. Intense sub-kilometer-scale boundary layer rolls observed in Hurricane Fran. *Science* **1998**, *280*, 555–557. [[CrossRef](#)]
25. Morrison, I.; Businger, S.; Marks, F.; Dodge, P.; Businger, J.A. An observational case for the prevalence of roll vortices in the hurricane boundary layer. *J. Atmos. Sci.* **2005**, *62*, 2662–2673. [[CrossRef](#)]
26. Zhu, P. A multiple scale modeling system for coastal hurricane wind damage mitigation. *Nat. Hazards* **2008**, *47*, 577–591. [[CrossRef](#)]
27. Zhu, P. Simulation and parameterization of the turbulent transport in the hurricane boundary layer by large eddies. *J. Geophys. Res. Atmos.* **2008**, *113*. [[CrossRef](#)]
28. Ellis, R.; Businger, S. Helical circulations in the typhoon boundary layer. *J. Geophys. Res. Atmos.* **2010**, *115*, D6. [[CrossRef](#)]
29. Foster, R. Signature of large aspect ratio roll vortices in synthetic aperture radar images of tropical cyclones. *Oceanography* **2013**, *26*, 58–67. [[CrossRef](#)]
30. Gao, K.; Ginis, I. On the equilibrium-state roll vortices and their effects in the hurricane boundary layer. *J. Atmos. Sci.* **2016**, *73*, 1205–1222. [[CrossRef](#)]
31. Gao, K.; Ginis, I.; Doyle, J.D.; Jin, Y. Effect of boundary layer roll vortices on the development of an axisymmetric tropical cyclone. *J. Atmos. Sci.* **2017**, *74*, 2737–2759. [[CrossRef](#)]
32. Tang, J.; Zhang, J.A.; Chan, P.; Hon, K.; Lei, X.; Wang, Y. A direct aircraft observation of helical rolls in the tropical cyclone boundary layer. *Sci. Rep.* **2021**, *11*, 18771. [[CrossRef](#)] [[PubMed](#)]
33. Willoughby, H.; Black, P. Hurricane Andrew in Florida: Dynamics of a disaster. *Bull. Am. Meteorol. Soc.* **1996**, *77*, 543–550. [[CrossRef](#)]
34. Montgomery, M.T.; Bell, M.M.; Aberson, S.D.; Black, M.L. Hurricane Isabel (2003): New insights into the physics of intense storms. Part I: Mean vortex structure and maximum intensity estimates. *Bull. Am. Meteorol. Soc.* **2006**, *87*, 1335–1348. [[CrossRef](#)]
35. Hendricks, E.A.; McNoldy, B.D.; Schubert, W.H. Observed inner-core structural variability in Hurricane Dolly (2008). *Mon. Weather Rev.* **2012**, *140*, 4066–4077. [[CrossRef](#)]
36. Wingo, S.M.; Knupp, K.R. Kinematic structure of mesovortices in the eyewall of Hurricane Ike (2008) derived from ground-based dual-Doppler analysis. *Mon. Weather Rev.* **2016**, *144*, 4245–4263. [[CrossRef](#)]
37. Wurman, J.; Kosiba, K. The role of small-scale vortices in enhancing surface winds and damage in Hurricane Harvey (2017). *Mon. Weather Rev.* **2018**, *146*, 713–722. [[CrossRef](#)]
38. Wu, L.; Liu, Q.; Li, Y. Prevalence of tornado-scale vortices in the tropical cyclone eyewall. *Proc. Natl. Acad. Sci. USA* **2018**, *115*, 8307–8310. [[CrossRef](#)]
39. Liu, Q.; Wu, L.; Qin, N.; Li, Y. Storm-Scale and Fine-Scale Boundary Layer Structures of Tropical Cyclones Simulated with the WRF-LES Framework. *J. Geophys. Res. Atmos.* **2021**, *126*, e2021JD035511. [[CrossRef](#)]
40. Chen, L.; Luo, Z.; Li, Y. Research advances on tropical cyclone landfall process. *Acta Meteorol. Sin.* **2004**, *5*, 541–549. (In Chinese)
41. Yang, M.J.; Zhang, D.L.; Tang, X.D.; Zhang, Y. A modeling study of Typhoon Nari (2001) at landfall: 2. Structural changes and terrain-induced asymmetries. *J. Geophys. Res. Atmos.* **2011**, *116*, D9. [[CrossRef](#)]
42. Wang, C.C.; Chen, Y.H.; Kuo, H.C.; Huang, S.Y. Sensitivity of typhoon track to asymmetric latent heating/rainfall induced by Taiwan topography: A numerical study of Typhoon Fanapi (2010). *J. Geophys. Res. Atmos.* **2013**, *118*, 3292–3308. [[CrossRef](#)]
43. Meng, Z.; Zhang, Y. On the squall lines preceding landfalling tropical cyclones in China. *Mon. Weather Rev.* **2012**, *140*, 445–470. [[CrossRef](#)]
44. Meng, Z.; Masashi, N.; Chen, L. A numerical study on the formation and development of island-induced cyclone and its impact on typhoon structure change and motion. *Acta Meteorol. Sin.* **1996**, *10*, 430–443.

45. Wu, C.-C. Numerical simulation of Typhoon Gladys (1994) and its interaction with Taiwan terrain using the GFDL hurricane model. *Mon. Weather Rev.* **2001**, *129*, 1533–1549. [[CrossRef](#)]
46. Hsu, L.-H.; Kuo, H.-C.; Fovell, R.G. On the geographic asymmetry of typhoon translation speed across the mountainous island of Taiwan. *J. Atmos. Sci.* **2013**, *70*, 1006–1022. [[CrossRef](#)]
47. Tang, C.K.; Chan, J.C. Idealized simulations of the effect of Taiwan and Philippines topographies on tropical cyclone tracks. *Q. J. R. Meteorol. Soc.* **2014**, *140*, 1578–1589. [[CrossRef](#)]
48. Xue, L.; Li, Y.; Xu, Y.L. Effect of Taiwan topography on the rapid intensification of typhoon Meranti (1010) passing by the Taiwan Strait. *Chin. J. Atmos. Sci.* **2015**, *39*, 789–801. (In Chinese)
49. Wu, C.-C.; Li, T.-H.; Huang, Y.-H. Influence of mesoscale topography on tropical cyclone tracks: Further examination of the channeling effect. *J. Atmos. Sci.* **2015**, *72*, 3032–3050. [[CrossRef](#)]
50. Xue, L.; Li, Y. The effect of mesoscale systems induced by the topography of Taiwan on the rapid intensification of typhoon Meranti (1010). *Chin. J. Atmos. Sci.* **2016**, *40*, 1107–1116. (In Chinese)
51. Jian, G.-J.; Wu, C.-C. A numerical study of the track deflection of Supertyphoon Haitang (2005) prior to its landfall in Taiwan. *Mon. Weather Rev.* **2008**, *136*, 598–615. [[CrossRef](#)]
52. Huang, Y.-H.; Wu, C.-C.; Wang, Y. The influence of island topography on typhoon track deflection. *Mon. Weather Rev.* **2011**, *139*, 1708–1727. [[CrossRef](#)]
53. Yeh, T.-C.; Hsiao, L.-F.; Chen, D.-S.; Huang, K.-N. A study on terrain-induced tropical cyclone looping in East Taiwan: Case study of Typhoon Haitang in 2005. *Nat. Hazards* **2012**, *63*, 1497–1514. [[CrossRef](#)]
54. Hu, S.; Li, Y.; Wei, N. Diagnostic analysis on Nari (0116) structure and intensity changes during its landfall process on Taiwan Island. *Chin. J. Atmos. Sci.* **2013**, *70*, 1006–1022. (In Chinese)
55. Gong, Y.; Li, Y.; Zhang, D.-L. A statistical study of unusual tracks of tropical cyclones near Taiwan Island. *J. Appl. Meteorol. Climatol.* **2018**, *57*, 193–206. [[CrossRef](#)]
56. Tan, C.; Fang, W. Mapping the wind hazard of global tropical cyclones with parametric wind field models by considering the effects of local factors. *Int. J. Disaster Risk Sci.* **2018**, *9*, 86–99. [[CrossRef](#)]
57. Duan, L.; Chen, L.; Xu, X. The numerical simulation on the impact of topography on the structure change and motion of tropical storm Fitow (0114). *Acta Meteorol. Sin.* **2006**, *64*, 591–605. (In Chinese)
58. Ji, C.; Xue, G.; Zhao, F.; Yu, Z.; Zhang, H. The numerical simulation of orographic effect on the rain and structure of typhoon Rananim during landfall. *Chin. J. Atmos. Sci.* **2007**, *31*, 12. (In Chinese)
59. Ni, X.; Zhang, Q.; Ma, D.; Wu, L.; Ren, F. Climatology and trends of tropical cyclone high wind in mainland China: 1959–2011. *J. Geophys. Res. Atmos.* **2015**, *120*, 12378–12393. [[CrossRef](#)]
60. Lu, Y.; Zhu, W.; Ren, F.; Fumin, R.; Xin, W. Changes of tropical cyclone high winds and extreme winds during 1980–2014 over China. *Clim. Change Res.* **2016**, *12*, 413–421. (In Chinese)
61. Huang, W.; Dong, S. Long-term and inter-annual variations of tropical cyclones affecting Taiwan region. *Reg. Stud. Mar. Sci.* **2019**, *30*, 100721. [[CrossRef](#)]
62. Liu, D.; Pan, N.; Huang, C.; Zheng, J.; He, C. Cluster analysis of tropical cyclones affecting the Taiwan Strait. *Int. J. Climatol.* **2019**, *39*, 3915–3931. [[CrossRef](#)]
63. Wu, Y.-S.; Teng, H.-F.; Chan, J.C.; Lee, C.-S. Long-term features of tropical cyclones affecting Taiwan. *Terr. Atmos. Ocean. Sci.* **2019**, *30*, 793–802. [[CrossRef](#)]
64. Hersbach, H.; Bell, B.; Berrisford, P.; Hirahara, S.; Horányi, A.; Muñoz-Sabater, J.; Nicolas, J.; Peubey, C.; Radu, R.; Schepers, D. The ERA5 global reanalysis. *Q. J. R. Meteorol. Soc.* **2020**, *146*, 1999–2049. [[CrossRef](#)]
65. Dullaart, J.C.; Muis, S.; Bloemendaal, N.; Aerts, J.C. Advancing global storm surge modelling using the new ERA5 climate reanalysis. *Clim. Dyn.* **2020**, *54*, 1007–1021. [[CrossRef](#)]
66. Bian, G.-F.; Nie, G.-Z.; Qiu, X. How well is outer tropical cyclone size represented in the ERA5 reanalysis dataset? *Atmos. Res.* **2021**, *249*, 105339. [[CrossRef](#)]
67. Zarzycki, C.M.; Ullrich, P.A.; Reed, K.A. Metrics for evaluating tropical cyclones in climate data. *J. Appl. Meteorol. Climatol.* **2021**, *60*, 643–660. [[CrossRef](#)]
68. Zhang, K.; Chan, K.T. An ERA5 global climatology of tropical cyclone size asymmetry. *Int. J. Climatol.* **2023**, *43*, 950–963. [[CrossRef](#)]
69. Slocum, C.J.; Razin, M.N.; Knaff, J.A.; Stow, J.P. Does ERA5 mark a new era for resolving the tropical cyclone environment? *J. Clim.* **2022**, *35*, 3547–3564. [[CrossRef](#)]
70. Han, Z.; Yue, C.; Liu, C.; Gu, W.; Tang, Y.; Li, Y. Evaluation on the applicability of ERA5 reanalysis dataset to tropical cyclones affecting Shanghai. *Front. Earth Sci.* **2022**, *16*, 1025–1039. [[CrossRef](#)]
71. Ying, M.; Zhang, W.; Yu, H.; Lu, X.; Feng, J.; Fan, Y.; Zhu, Y.; Chen, D. An overview of the China Meteorological Administration tropical cyclone database. *J. Atmos. Ocean. Technol.* **2014**, *31*, 287–301. [[CrossRef](#)]
72. Sampson, C.R.; Fukada, E.M.; Knaff, J.A.; Strahl, B.R.; Brennan, M.J.; Marchok, T. Tropical cyclone gale wind radii estimates for the western North Pacific. *Weather Forecast.* **2017**, *32*, 1029–1040. [[CrossRef](#)]
73. Sampson, C.R.; Goerss, J.S.; Knaff, J.A.; Strahl, B.R.; Fukada, E.M.; Serra, E.A. Tropical cyclone gale wind radii estimates, forecasts, and error forecasts for the western North Pacific. *Weather Forecast.* **2018**, *33*, 1081–1092. [[CrossRef](#)]
74. Knaff, J.A.; Sampson, C.R.; Musgrave, K.D. Statistical tropical cyclone wind radii prediction using climatology and persistence: Updates for the western North Pacific. *Weather Forecast.* **2018**, *33*, 1093–1098. [[CrossRef](#)]

75. Sampson, C.R.; Knaff, J.A. A consensus forecast for tropical cyclone gale wind radii. *Weather Forecast.* **2015**, *30*, 1397–1403. [[CrossRef](#)]
76. Knaff, J.A.; Sampson, C.R.; Kucas, M.E.; Slocum, C.J.; Brennan, M.J.; Meissner, T.; Ricciardulli, L.; Mouche, A.; Reul, N.; Morris, M. Estimating tropical cyclone surface winds: Current status, emerging technologies, historical evolution, and a look to the future. *Trop. Cyclone Res. Rev.* **2021**, *10*, 125–150. [[CrossRef](#)]
77. Pun, I.F.; Knaff, J.A.; Sampson, C.R. Uncertainty of tropical cyclone wind radii on sea surface temperature cooling. *J. Geophys. Res. Atmos.* **2021**, *126*, e2021JD034857. [[CrossRef](#)]
78. Chen, J.-M.; Lu, F.-C.; Kuo, S.-L.; SHIH, C.-F. Summer climate variability in Taiwan and associated large-scale processes. *J. Meteorol. Soc. Jpn. Ser. II* **2005**, *83*, 499–516. [[CrossRef](#)]
79. Chen, J.-M.; Li, T.; Shih, C.-F. Tropical cyclone- and monsoon-induced rainfall variability in Taiwan. *J. Clim.* **2010**, *23*, 4107–4120. [[CrossRef](#)]
80. Wu, C.-C.; Kuo, Y.-H. Typhoons affecting Taiwan: Current understanding and future challenges. *Bull. Am. Meteorol. Soc.* **1999**, *80*, 67–80. [[CrossRef](#)]
81. Oliver, M.A.; Webster, R. Kriging: A method of interpolation for geographical information systems. *Int. J. Geogr. Inf. Syst.* **1990**, *4*, 313–332. [[CrossRef](#)]
82. Brand, S. Very large and very small typhoons of the western North Pacific Ocean. *J. Meteorol. Soc. Jpn. Ser. II* **1972**, *50*, 332–341. [[CrossRef](#)]
83. Merrill, R.T. A Comparison of Large and Small Tropical Cyclones. *Mon. Weather Rev.* **1984**, *112*, 1408–1418. [[CrossRef](#)]
84. Xue, L.; Li, Y.; Wang, B.L.; Zhou, R.W. Characteristics of Tropical Cyclone-Induced Low-Level Wind Fields over Hainan. *Clim. Environ. Res.* **2018**, *23*, 299–310. (In Chinese)
85. Knaff, J.A.; Longmore, S.P.; Molenaar, D.A. An objective satellite-based tropical cyclone size climatology. *J. Clim.* **2014**, *27*, 455–476. [[CrossRef](#)]
86. Chan, K.T.; Chan, J.C. Impacts of initial vortex size and planetary vorticity on tropical cyclone size. *Q. J. R. Meteorol. Soc.* **2014**, *140*, 2235–2248. [[CrossRef](#)]
87. Tao, D.; Bell, M.; Rotunno, R.; Van Leeuwen, P.J. Why do the maximum intensities in modeled tropical cyclones vary under the same environmental conditions? *Geophys. Res. Lett.* **2020**, *47*, e2019GL085980. [[CrossRef](#)]
88. Wang, Y. Structure and formation of an annular hurricane simulated in a fully compressible, nonhydrostatic model—TCM4. *J. Atmos. Sci.* **2008**, *65*, 1505–1527. [[CrossRef](#)]
89. Maclay, K.S.; DeMaria, M.; Haar, T.H.V. Tropical cyclone inner-core kinetic energy evolution. *Mon. Weather Rev.* **2008**, *136*, 4882–4898. [[CrossRef](#)]
90. Wang, Y. How do outer spiral rainbands affect tropical cyclone structure and intensity? *J. Atmos. Sci.* **2009**, *66*, 1250–1273. [[CrossRef](#)]
91. Xu, J.; Wang, Y. Sensitivity of tropical cyclone inner-core size and intensity to the radial distribution of surface entropy flux. *J. Atmos. Sci.* **2010**, *67*, 1831–1852. [[CrossRef](#)]
92. Wang, S.; Toumi, R. Impact of dry midlevel air on the tropical cyclone outer circulation. *J. Atmos. Sci.* **2019**, *76*, 1809–1826. [[CrossRef](#)]
93. Martinez, J.; Nam, C.C.; Bell, M.M. On the contributions of incipient vortex circulation and environmental moisture to tropical cyclone expansion. *J. Geophys. Res. Atmos.* **2020**, *125*, e2020JD033324. [[CrossRef](#)]
94. Ditchek, S.D.; Molinari, J.; Corbosiero, K.L.; Fovell, R.G. An objective climatology of tropical cyclone diurnal pulses in the Atlantic basin. *Mon. Weather Rev.* **2019**, *147*, 591–605. [[CrossRef](#)]
95. Rappin, E.D.; Nolan, D.S. The effect of vertical shear orientation on tropical cyclogenesis. *Q. J. R. Meteorol. Soc.* **2012**, *138*, 1035–1054. [[CrossRef](#)]
96. Zhou, Y.; Matyas, C.; Li, H.; Tang, J. Conditions associated with rain field size for tropical cyclones landfalling over the Eastern United States. *Atmos. Res.* **2018**, *214*, 375–385. [[CrossRef](#)]
97. Chen, B.-F.; Davis, C.A.; Kuo, Y.-H. Effects of low-level flow orientation and vertical shear on the structure and intensity of tropical cyclones. *Mon. Weather Rev.* **2018**, *146*, 2447–2467. [[CrossRef](#)]
98. Chen, B.-F.; Davis, C.A.; Kuo, Y.-H. Examination of the combined effect of deep-layer vertical shear direction and lower-tropospheric mean flow on tropical cyclone intensity and size based on the ERA5 reanalysis. *Mon. Weather Rev.* **2021**, *149*, 4057–4076.
99. Finocchio, P.M.; Rios-Berrios, R. The intensity- and size-dependent response of tropical cyclones to increasing vertical wind shear. *J. Atmos. Sci.* **2021**, *78*, 3673–3690. [[CrossRef](#)]
100. Wang, S.; Toumi, R. Recent tropical cyclone changes inferred from ocean surface temperature cold wakes. *Sci. Rep.* **2021**, *11*, 22269. [[CrossRef](#)]
101. Bruneau, N.; Wang, S.; Toumi, R. Long memory impact of ocean mesoscale temperature anomalies on tropical cyclone size. *Geophys. Res. Lett.* **2020**, *47*, e2019GL086165. [[CrossRef](#)]
102. Yang, N.; Li, Y.; Chan, J.C.; Cheung, K.K.; Ye, L.; Wu, Y. Vertical variation of tropical cyclone size in the western North Pacific. *Int. J. Climatol.* **2022**, *42*, 4424–4444. [[CrossRef](#)]
103. Chen, J.; Chavas, D.R. The transient responses of an axisymmetric tropical cyclone to instantaneous surface roughening and drying. *J. Atmos. Sci.* **2020**, *77*, 2807–2834. [[CrossRef](#)]
104. Chen, J.; Chavas, D.R. Can existing theory predict the response of tropical cyclone intensity to idealized landfall? *J. Atmos. Sci.* **2021**, *78*, 3281–3296. [[CrossRef](#)]

105. Hlywiak, J.; Nolan, D.S. The response of the near-surface tropical cyclone wind field to inland surface roughness length and soil moisture content during and after landfall. *J. Atmos. Sci.* **2021**, *78*, 983–1000. [[CrossRef](#)]
106. Hlywiak, J.; Nolan, D.S. The evolution of asymmetries in the tropical cyclone boundary layer wind field during landfall. *Mon. Weather Rev.* **2022**, *150*, 529–549. [[CrossRef](#)]

Disclaimer/Publisher's Note: The statements, opinions and data contained in all publications are solely those of the individual author(s) and contributor(s) and not of MDPI and/or the editor(s). MDPI and/or the editor(s) disclaim responsibility for any injury to people or property resulting from any ideas, methods, instructions or products referred to in the content.